JGR Oceans

RESEARCH ARTICLE
10.1029/2023JC019755

Impact of a Large Shallow Semi-Enclosed Lagoon on Freshwater Exchange Across an Inlet Channel

Shinichiro Kida[1], Kiyoshi Tanaka[2], Tomonori Isada[3], and Tomohiro Nakamura[4]

[1]Research Institute for Applied Mechanics, Kyushu University, Kasuga, Japan, [2]Atmosphere and Ocean Research Institute, The University of Tokyo, Otsuchi, Japan, [3]Akkeshi Marine Station, Field Science Center for Northern Biosphere, Hokkaido University, Akkeshi, Japan, [4]Pan-Okhotsk Research Center, Institute of Low Temperature Science, Hokkaido University, Sapporo, Japan

Key Points:

- A large lagoon with a narrow inlet induces strong tidal pumping across the channel, in turn generating plumes in the ocean and lagoon
- Mixing is enhanced as the sharp salinity front formed within the shallow lagoon moves across the sloping bottom during the ebb phase
- Tidal pumping induces more freshwater exchange than estuarine circulation when the estuarine Richardson number is below unity

Supporting Information:

Supporting Information may be found in the online version of this article.

Correspondence to:

S. Kida,
kida@riam.kyushu-u.ac.jp

Citation:

Kida, S., Tanaka, K., Isada, T., & Nakamura, T. (2024). Impact of a large shallow semi-enclosed lagoon on freshwater exchange across an inlet channel. *Journal of Geophysical Research: Oceans*, *129*, e2023JC019755. https://doi.org/10.1029/2023JC019755

Received 19 FEB 2023
Accepted 7 DEC 2023

Abstract The impact of a large shallow semi-enclosed lagoon on freshwater exchange across an inlet channel is investigated using an idealized numerical model. Lagoons are often found between a river mouth and the ocean; we focus on those where the river discharge rate is small and the inlet channel is narrower and deeper than the lagoon. Tides generate freshwater and oceanic-water plumes across the channel; a stratified freshwater plume forms in the ocean from the late ebb to early flood phase, while a vertically well-mixed oceanic-water plume forms in the lagoon from the late flood to early ebb phase. The shallow depth of the lagoon increases the flow speed of the oceanic-water plume, which results in the formation of a sharp and vertically well-mixed salinity front within the lagoon. When this front moves toward the ocean during the ebb phase, vertical mixing increases where the bathymetry deepens and freshwater encounters oceanic water below. Without a dredged bottom slope, the impact of mixing would be greatly reduced within the shallow lagoon and channel, as the shallow depth would limit the subsurface intrusion of oceanic water. The narrow channel further causes the flow to converge and accelerate, enhancing both internal shear-driven and bottom boundary-layer mixing at the channel and increasing freshwater plume thickness where it enters the ocean. Sensitivity experiments showed that the role of tidal pumping in freshwater exchange across the channel increases when the lagoon area and tidal mixing increase and when the estuarine Richardson number decreases.

Plain Language Summary Freshwater outflows from estuaries play an important role in supporting coastal marine environments. Large shallow lagoons are often found at river mouths with an inlet channel; this study uses idealized numerical model experiments to investigate how lagoons affect freshwater exchange across an inlet channel where the river discharge rate is low. Freshwater exchange often results in estuarine circulation wherein freshwater enters the ocean near the surface, while oceanic water intrudes into the estuary near the bottom, with weaker circulation expected for a shallow environment. We find that large lagoons force strong tidal flows across the channel, enhancing mixing between freshwater and oceanic water, especially during the ebb phase. Due to the fast flow generated over the shallow lagoon, mixing occurs when freshwater in the lagoon moves across a sloping bottom and interacts with oceanic water below. Freshwater outflow becomes thicker and tidally pulsed plumes are generated.

1. Introduction

Numerous small rivers drain into the sea along coastlines around the globe. Small rivers are typically less than a kilometer wide and have discharge rates of a few 10 $m^3\ s^{-1}$, thus several orders of magnitude smaller than those of continental-scale rivers. Nonetheless, small rivers play important roles in supporting local productivity and the marine environment as sources of nutrients and pollutants, among other materials (Bauer et al., 2013; Izett & Fennel, 2018). Since satellites such as Landsat 8 and Sentinel 2 began to provide near-coast data at high spatial resolutions, interest in the behavior of small rivers has grown (Isada et al., 2022; Pahlevan et al., 2020). When multiple rivers are located near each other, a low-salinity barrier can form along the coastline over a long distance (Carmack et al., 2015). Discharge rates increase by multiple orders of magnitude after heavy rainstorms, enabling the transport of freshwater and sediments over a much larger area than under normal conditions (Warrick & Fong, 2004).

Studies on the fate of freshwater from small rivers have been limited, in part due to the difficulty of observing its strong temporal variations. The role of advection is likely important, because the flow typically has a Kelvin

number of less than 1, as the across-shore length scale of the flow is smaller than the baroclinic deformation radius (Garvine, 1995). Using a numerical model, Basdurak et al. (2020) showed that buoyancy-controlled small rivers with discharge rates (Q) of 10–100 $m^3\ s^{-1}$ create freshwater outflows that expand radially as surface-oriented plumes when temporally averaged, while advection-controlled small rivers create freshwater outflows that are thinner and well mixed. Tides and waves enhance mixing between riverine and oceanic waters, limiting the dispersion of low-salinity signals to the areas near river mouths (Iwanaka & Isobe, 2018; Rodriguez et al., 2018). For mid-size rivers with high discharge rates ($Q > 100\ m^3\ s^{-1}$), heads associated with gravity currents and Kelvin–Helmholtz-like billows have been observed beneath the riverine water, implying the occurrence of shear-driven mixing (McPherson, et al., 2020; Nash & Moum, 2005). Spicer et al. (2021) showed the strong influence of bottom-generated tidal mixing during the ebb phase for tidally pulsed freshwater outflows on the oceanic slope. Strong tidal outflows can generate tidal plume fronts (Luketina & Imberger, 1987) and affect the propagation speed of these fronts (Kilcher & Nash, 2010).

Previous idealized modeling studies on freshwater outflows have focused primarily on the behavior of freshwater on the oceanic slope and simplified the river into a straight, flat, and narrow pathway directly connected to the ocean. For such modeled outflows, freshwater enters the oceanic slope during the ebb phase and remains stagnant near the river mouth during the flood phase and strong mixing occurs during the ebb phase (Spicer et al., 2021). However, a shallow semi-enclosed lagoon that covers an area larger than the river pathway is occasionally located between the river mouth and the ocean, such as along the coast adjacent to wetlands. A narrow inlet channel then connects the lagoon to the ocean, which is deeper than the lagoon due to dredging or rapid flow, and essentially acts as a river mouth to the ocean. Hench et al. (2002) showed that in the absence of a density difference between the estuary and the ocean, the flow that occurs at the inlet channel reverses symmetrically with the tidal cycle, filling and emptying the lagoon as sea surface height changes.

Studies on the impact of a lagoon on freshwater exchange across an inlet channel have focused primarily on when mid- or large-scale rivers discharge with high rates ($Q > 100\ m^3\ s^{-1}$). In such cases, geostrophically balanced flow is established in the channel, with freshwater occupying the surface for most of the tidal cycle (e.g., Kapolnai et al., 1996; Wheless & Valle-Levinson, 1996). An anticyclonic plume is established in the ocean, which becomes a coastal buoyant current with the coastline to its right in the Northern Hemisphere. With lateral constriction in the channel, asymmetry arises in the flow at the inlet channel between the ebb and flood phases, when a density gradient is present; jet-like flow forms during the ebb phase, while weakly barotropic flow forms during the flood phase. Such exchange flows driven across the channel are termed tidal pumping and play an equally important role in transporting freshwater to the ocean as the estuarine circulation (e.g., Chen et al., 2012; MacCready, 2004; Stommel & Farmer, 1952). For an estuary affected by a mid-size river discharge, Ralston et al. (2010) showed that the ebb phase is the dominant phase of mixing and induces internal shear-driven and bottom boundary-layer mixing to occur as the salt wedge moves toward the ocean.

However, the dynamics and mechanism of mixing are still unknown for freshwater exchange across the inlet channel of a shallow lagoon (about 1 m in depth), when the discharge is small. With a typical Kelvin number less than 1, tidal flows likely play a more important role, causing water-mass properties at the inlet channel to change more dramatically with the tidal cycle. The lengths of the tidal excursion are also more likely to become similar to the size of the lagoon and make tidal pumping an important component of the freshwater exchange across the channel (Chen et al., 2012). Bathymetry also provides strong control over flow speeds in shallow environments, and thus freshwater outflow is likely sensitive to the depths of the lagoon and the inlet channel; however, previous studies on flows through inlet channels have kept the depth of the channel and the estuary constant (e.g., Hench & Luettich, 2003). A difference in these depths may cause the magnitude of mixing to change, affecting the water-mass properties and the strength of the freshwater exchange. Bathymetric changes within an estuary enhance mixing (Ralston et al., 2010).

This study uses an idealized numerical model to investigate how a large shallow semi-enclosed lagoon affects the dynamics of freshwater exchange across an inlet channel. Section 2 describes the basic setup of the experiments and the observational data used for comparisons. Model results from a control experiment are presented in Section 3 and sensitivity experiments are presented in Section 4, with the discussion in Section 5. Section 6 presents a summary.

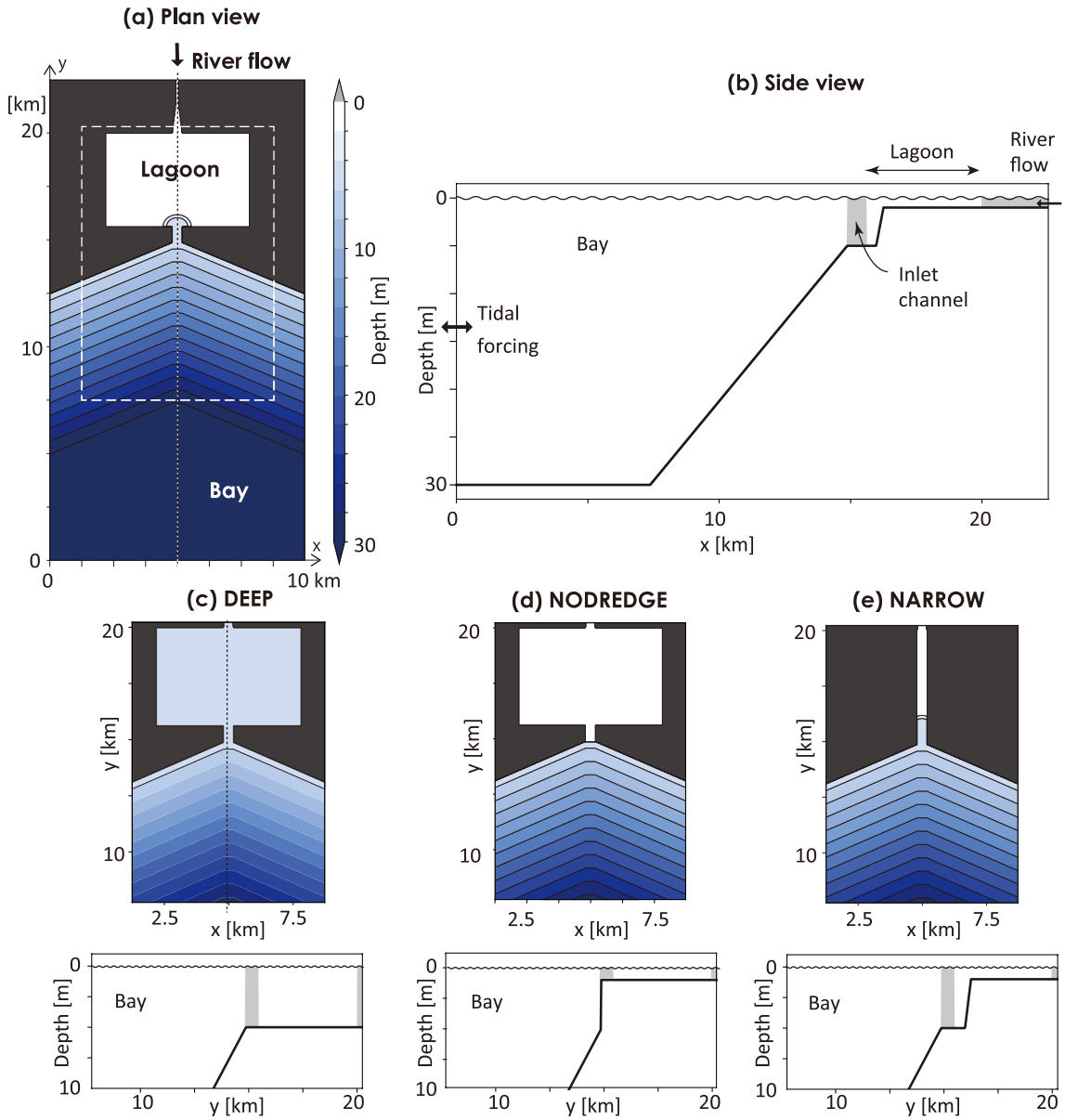

Figure 1. Schematic diagram of the model setup. (a) Plan view of the bottom bathymetry used for the control experiment. River flow is forced at the northern boundary. (b) Side view of the bottom bathymetry along the dotted line in (a), representing $x = 5$ km. Tides are forced along the southern boundary. Gray shading indicates the locations of the inlet channel and narrow pathway. (c) Bottom bathymetry within the white dashed box in (a) for DEEP, (d) NODREDGE, and (e) NARROW. The upper panels show the plan view. The lower panels show the side view along the dotted line in the upper panel of (c), representing $x = 5$ km near the surface.

2. Numerical Model Setup and Observations

2.1. Numerical Model Setup

2.1.1. Control Experiment

An idealized model of freshwater outflow through a lagoon was constructed using KINACO, a free-surface z-level vertical coordinate non-hydrostatic model (Matsumura & Hasumi, 2008). The model domain includes an estuary with a narrow pathway, a rectangular lagoon, and a bay (Figure 1a). To focus on the effect of lagoon area on the freshwater exchange across the inlet channel, we distinguish the narrow pathway and lagoon area of the estuary based on their geometric differences. The model parameters resemble those of the Akkeshi Estuary, an ideal location where there is an isolated shallow lagoon, with a narrow inlet channel and small discharge; we compare

the model results with observations later. The area of the lagoon (A) is 25 km^2 and the width of the inlet channel (W) is 400 m. Both the narrow pathway and the lagoon are 1 m deep, which increases to 5 m near the channel with a slope of 0.11 and remains at 5 m within the channel. The depth increases from 5 to 30 m from the channel to the bay, with a slope of 0.04. The vertical resolution is 0.25 m in the uppermost layer and increases to 0.10 m at 1 m depth to better resolve the near-bottom flows of the estuary. Then the resolution is gradually reduced to 2 m at a depth of 30 m. The horizontal resolution is 25 m; thus, while the model is non-hydrostatic, its resolution is not sufficient to resolve the mixing process explicitly. Therefore, we use generic length-scale vertical mixing parameterization (Umlauf & Burchard, 2003) to estimate the vertical viscosity coefficient (A_Z) and vertical diffusivity coefficient (K_Z) with a background value of 1×10^{-6} m^2 s^{-1}. This value reflects the no-wind condition and was used by Ralston et al. (2010). Sensitivity to the magnitude of the background viscosity and diffusivity coefficients is discussed in Section 6. A centered fourth-order advection scheme is used for momentum and a third-order upwind bias advection scheme is used for tracers. The model results are not overly sensitive to the selected advection scheme. Smagorinsky-type lateral viscosity is used with a constant of 0.1. Quadratic bottom drag is used for bottom stress, with a constant drag coefficient of 5.5×10^{-3}. Hereafter, the positive x and y directions are referred to as eastward and northward, respectively.

River flow is prescribed at the northern boundary with a vertically uniform southward velocity of 0.18 m s^{-1} and a width of 100 m. The discharge rate (Q) is 18 m^3 s^{-1} and the salinity (S) values of the incoming water and ambient oceanic water are 22 and 32 PSU, respectively, which are similar to observations (Ding, 2020; Isada et al., 2021). The salinity of the incoming water is non-zero, because the narrow pathway in the model is too short to reproduce mixing that takes place further upstream. Temperature is uniform across the model domain and constant over time. A linear equation of state is used for density with a haline contraction coefficient of $\beta = 8.0 \times 10^{-4}$.

Tides are forced along the southern boundary as vertically uniform meridional flow which varies semidiurnally, as follows:

$$v_{SB} = v_a \sin \frac{2\pi t}{T} - v_b, \tag{1}$$

where t is time, T is the semidiurnal tidal period (12 hr), v_a is 1.5×10^{-2} m s^{-1}, and v_b is the background flow of 6.0×10^{-5} m s^{-1}, which offsets the forced river discharge at the northern boundary. The sea-level change ($\Delta\eta$) induced by tidal forcing is approximately 0.25 m, a realistic value that avoids numerical instability caused by excessive thinning of the uppermost layer. The salinity and flow fields are restored to 32 PSU (oceanic value) and v_{SB} over a time scale of 6 hr within 5 km of the southern boundary. Wind stress is set to zero.

River flow alone would create steady freshwater outflow through the channel of approximately $v_r = \frac{Q}{HW} = 9 \times 10^{-3}$ m s^{-1}, assuming spatially uniform flow. The magnitude of the tidally forced flow in the channel (v_c) can be roughly estimated based on mass balance. The total mass input induced by the flood tide is approximately $\frac{v_c}{2} \cdot H \cdot W \cdot \frac{\mathrm{T}}{2}$, where H is the channel depth and W is the channel width. This value should equal $A \bullet \Delta\eta$, the total mass input necessary to raise the sea level of the lagoon by $\Delta\eta$. Therefore,

$$v_c = \frac{4A \cdot \Delta\eta}{T \cdot H \cdot W} \tag{2}$$

which is equal to 0.28 m s^{-1} for the parameter values listed above. Equation 2 assumes that the tidal prism is controlled by the area of the lagoon (A). Flow through the channel is the sum of v_r and v_c; as v_c is one order of magnitude larger than v_r, flow is controlled by tides and reverses every tidal cycle.

The model setup described above is the control experiment. The model is integrated for 20 days so that the flow and salinity fields reach a quasi-steady state for each tidal cycle. Model results are averaged hourly or over the semidiurnal tidal cycle on the last tidal cycle of the simulation (day 20) unless otherwise noted.

2.1.2. Sensitivity Experiments

To clarify the dynamics of freshwater exchange across the channel, six sensitivity experiments are used that vary the model parameters in the control experiment (Table 1). Sensitivity to tides is examined by varying the tidal elevation ($\Delta\eta$) to 0.31, 0.18, 0.13, 0.08, or 0.0 m, and the experiment with no tides (0.0 m) is called NOTIDE. Sensitivity to lagoon depth (D_E) is examined by increasing D_E to 5 m, equal to the depth of the channel, and

Table 1
List of Parameters Used for the Sensitivity Experiments

Experiment Name	Parameters
Tidal forcing	$\Delta\eta$ = 0.31, 0.18, 0.13, 0.08, 0.0 (NOTIDE) [m]
Lagoon depth (DEEP)	D_E = 5.0 [m]
Channel depth (NODREDGE)	H = 1.0 [m]
Lagoon area	A = 12, 1.8 (NARROW) [km^2]
Coriolis (CORI)	$f = 1 \times 10^{-4}$ [s^{-1}]
Large scale (LARGE)	$f = 1 \times 10^{-4}$ [s^{-1}], A = 2,500 [km^2], Q = 180 [m^3 s^{-1}], W = 4 [km]

Note. The basic model parameters for the control experiment are $\Delta\eta$ = 0.25 m, D_E = 1.0 m, H = 5.0 m, A = 25.0 km^2, f = 0.0 s^{-1}, Q = 18 m^3 s^{-1}, and W = 400 m. Only parameters that were changed from the control experiment are listed.

is called DEEP (Figure 1c). Sensitivity to channel depth (H) is examined by decreasing H to 1.0 m, equal to the depth of the lagoon, and thus allowing no dredging of the channel; this experiment is called NODREDGE (Figure 1d). Sensitivity to lagoon area (A) is examined by decreasing A to 12 or 1.8 km^2, by reducing the zonal length of the lagoon while keeping the meridional length constant. At A = 1.8 km^2, the lagoon becomes a straight channel connecting the river mouth to the bay; this experiment is called NARROW (Figure 1e). Sensitivity to Earth's rotation is examined by adding a Coriolis term to the horizontal momentum equation of the model with the Coriolis parameter f set to 1×10^{-4} s^{-1} and is called CORI. Sensitivity to the spatial scale of freshwater exchange is examined by increasing the lateral domain length scale and the river discharge by one order of magnitude to A = 2,500 km^2, Q = 180 m^3 s^{-1}, and W = 4 km. The horizontal resolution is set to 250 m. This experiment is called LARGE.

2.2. Observational Data

Model results are compared to observations in the Akkeshi Estuary in Hokkaido, Japan (Figure 2a). The estuary is approximately 1 m deep. The inlet channel is 5 m deep on average and approximately 400 m wide at its narrowest point, representing the case of a shallow semi-enclosed lagoon with a narrow inlet channel. The river discharge rate is approximately 18 m^3 s^{-1} (Ding, 2020), with a salinity of approximately 22 PSU near the river mouth (Isada et al., 2021). Freshwater flows out through the lagoon and channel to enter Akkeshi Bay, where it interacts with the Oyashio Current, the western boundary current of the North Pacific subpolar gyre.

To capture the variation in flow and water-mass properties near the surface and bottom of the channel, observations were conducted in the middle of the channel from 11 a.m. on 12 September to 9 a.m. on 14 September 2018 (Figures 2b and 2c). Temperature-salinity loggers (INFINITY-CT; JFE-Advantech) and electromagnetic current meters (INFINITY-EM; JFE-Advantech) were bottom-anchored near the channel and instruments were placed at 0.5 m below the sea surface and 1 m above the seafloor. The ocean depth was 9.9 m at the time of deployment. Measurements were taken at 10-min intervals for 46 hr to capture the main semidiurnal tidal signal. Atmospheric conditions were moderate during the observation period, with an average southerly wind speed of 3.4 m s^{-1}, diurnal temperature changes within 9°C, and no precipitation. These data were obtained from the weather observatory of the Japan Meteorological Agency located in Ota, Hokkaido (Japan Meteorological Agency, 2023); this observatory is closest to our study area. Therefore, we consider the observations to show a reasonable representation of freshwater exchange across the inlet channel.

3. Simulated Freshwater Outflow and Comparison to Observations

3.1. Control Experiment

Model results from the control experiment show the flow and salinity fields alternating with the tidal cycle; a freshwater plume forms within the bay and an oceanic-water plume forms within the lagoon (Figures 3a–3d). Hereafter, we refer to hours 0–6 as the flood phase and hours 6–12 as the ebb phase. During the early flood phase (hours 0–3), a radially expanding freshwater plume is present in the bay (Figures 3a and 4a). The head of the plume extends a few kilometers into the interior of the bay, maintaining its low salinity of approximately 29

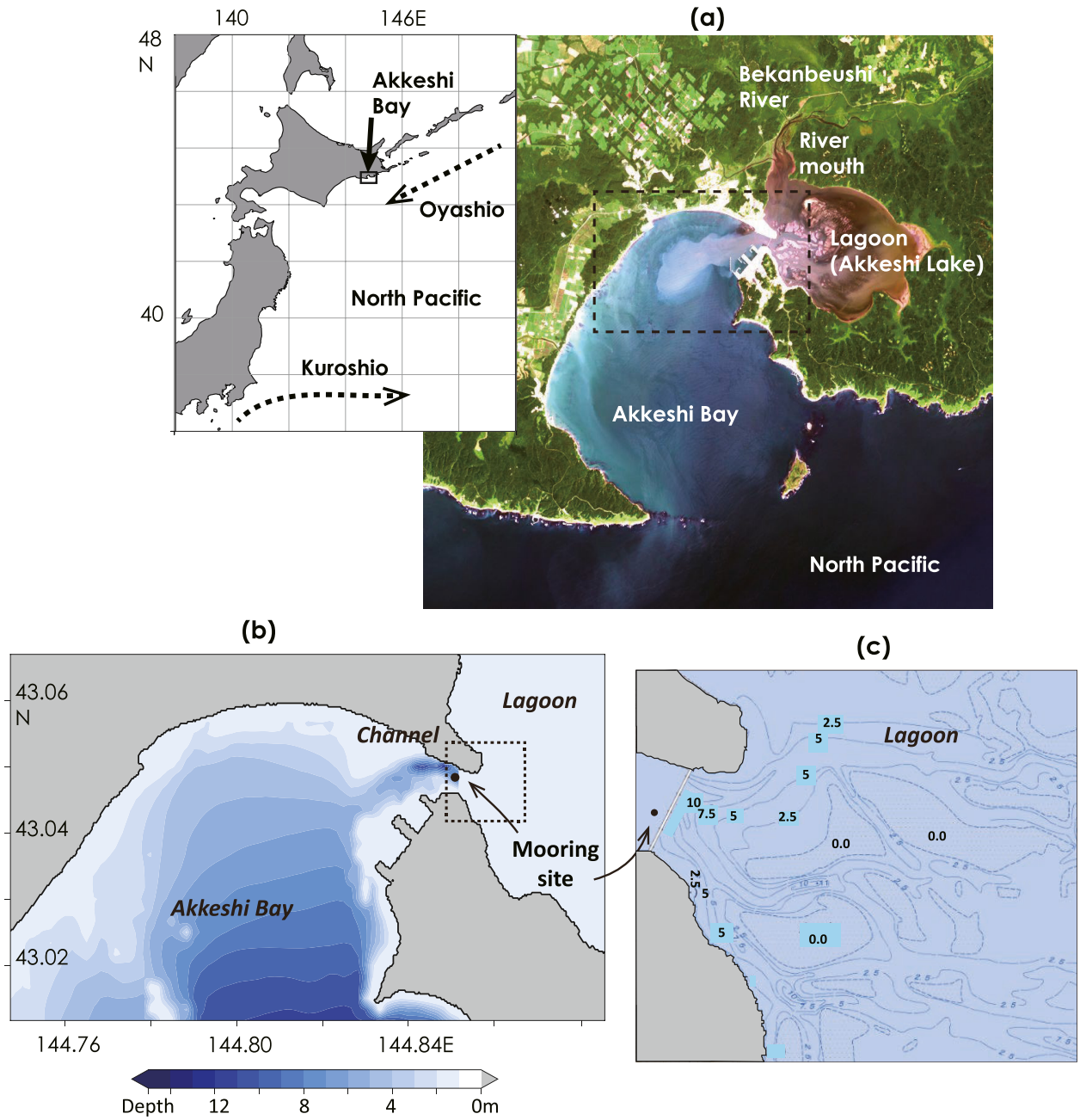

Figure 2. (a) Location of Akkeshi Bay. (b) RGB image of Akkeshi Estuary derived from Landsat 8 (USGS/NASA) observations on 3 August 2019, showing a freshwater plume entering the bay. The location of the region is shown in the top left inset. (b) Bathymetry is indicated as color for the region of Akkeshi Bay within the black dashed box in (a). Note that bathymetry is shown only within the bay due to the lack of digital data. The solid dot represents the location where measurements were taken in September 2018. (c) Bathymetry of the lagoon within the black dotted box in (c) from the Global Map published by the Geospatial Information Authority of Japan. Blue lines are bathymetric contours.

PSU. In the channel, freshwater occupies nearly half of the depth profile, with surface salinity as low as 27.5 PSU. Oceanic water below the freshwater layer is directed toward the lagoon, aligning with the direction of flow expected during the flood phase. The lagoon is fresh from the surface to the bottom. During the late flood phase (hours 3–6), a thick oceanic-water plume forms in the lagoon with a sharp salinity front (Figures 3b and 4b). The water column is vertically well mixed, possibly due to bottom boundary-layer mixing. The freshwater plume in the bay, meanwhile, is thin and more laterally dispersed. During the early ebb phase (hours 6–9), flow in the channel is toward the bay, but the channel remains occupied by oceanic water that entered the lagoon during the late

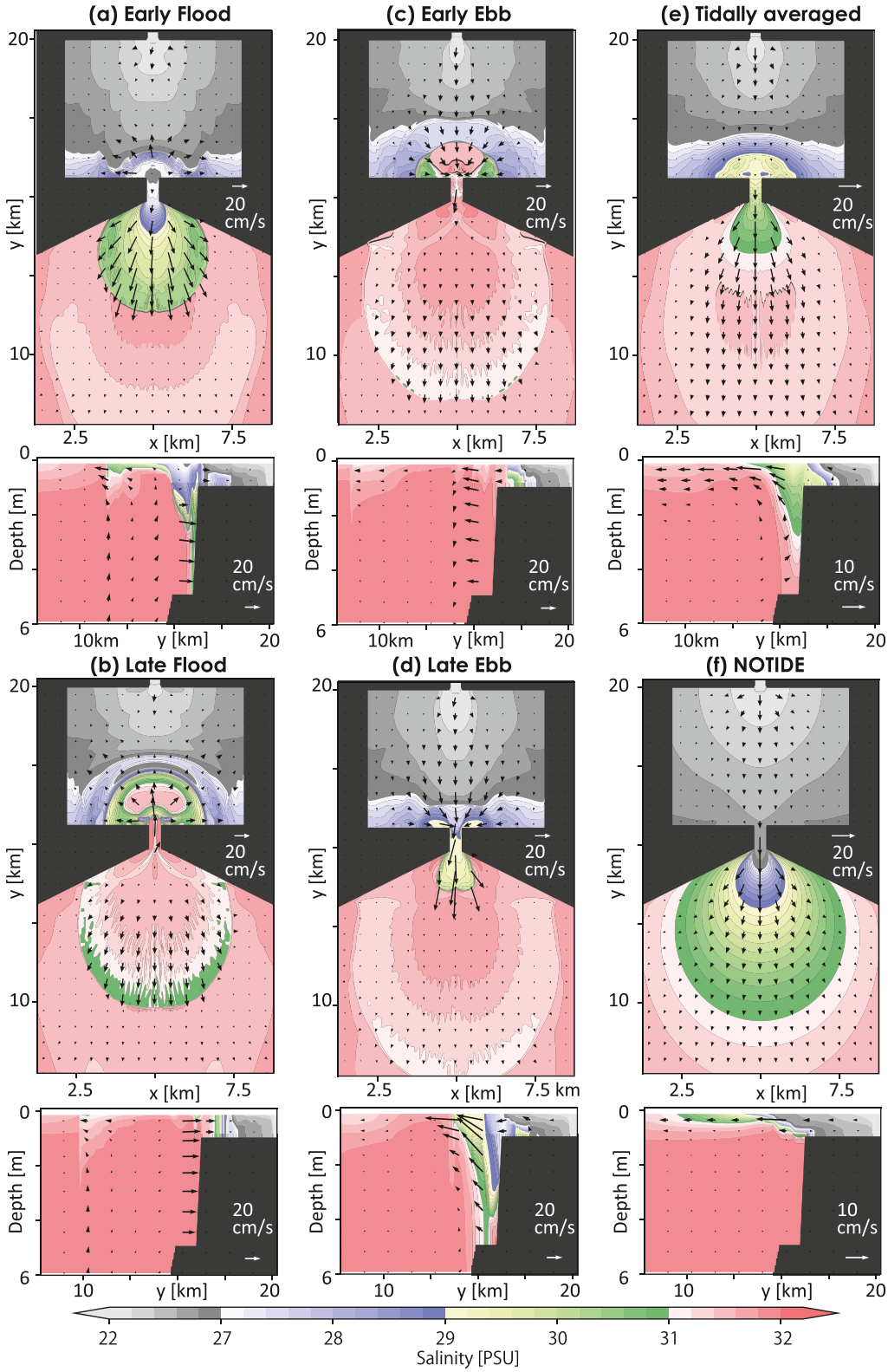

Figure 3. Surface flow and salinity fields for the control experiment during (a) the early flood phase (hour 1), (b) the late flood phase (hour 4), (c) early ebb phase (hour 7), (d) late ebb phase (hour 10), (e) tidally averaged, and (f) 12-hr average for NOTIDE. The upper panels represent the surface within the white dashed box in Figure 2a and the lower panels show a vertical cross-section along the black dotted line within the box.

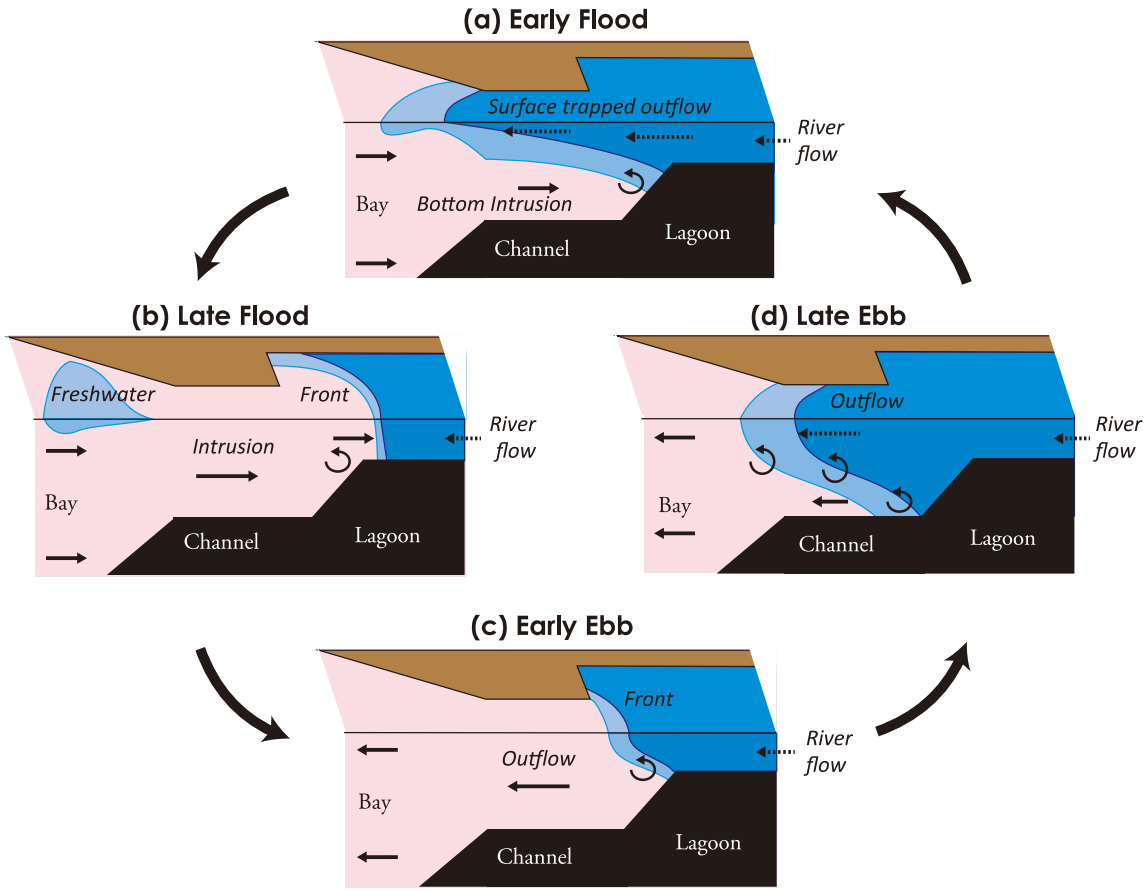

Figure 4. Schematic of freshwater exchange across the channel over the tidal cycle: (a) early flood phase, (b) late flood phase, (c) early ebb phase, and (d) late ebb phase. Freshwater and oceanic water are indicated with blue and pink shading, respectively.

flood phase (Figures 3c and 4c). Stratification is re-established in the channel when the salinity front is advected toward the channel and converges. In the late ebb phase (hours 9–12), freshwater occupies the channel as a thick water column that nearly reaches the bottom (Figures 3d and 4d) and the salinity front becomes the head of the freshwater plume that radially expands within the bay in the early flood phase (Figures 3a and 4a).

The time series of along-channel velocity and salinity at the surface and bottom of the channel show differences in the dynamics between the oceanic water and freshwater plumes. When intrusion of oceanic water occurs in the late flood phase, flow speed and salinity at the surface and bottom are similar and change synchronously (Figures 5b and 5c), which indicates that oceanic water is entering the lagoon as barotropic flow with a vertically well-mixed water column. This structure is maintained until the early ebb phase, and oceanic water occupies the channel until an abrupt decrease in salinity occurs and surface flow strengthens toward the bay. As the salinity front is located away from the channel when flow switches from the flood to ebb phase (Figures 3b and 3c), changes in salinity in the channel lag the change in flow by about 6 hr. Bottom salinity, on the other hand, is low only during the late ebb phase. When the tide switches from the ebb to flood phase, oceanic water intrusion begins near the bottom, but low-salinity water still occupies the surface and freshwater outflow continues. This time-series pattern is consistent with our results for the vertical cross-section of salinity in the early flood phase, when freshwater enters the bay near the surface and intrusion of oceanic water occurs near the bottom (Figures 3a and 4a). An abrupt increase in surface salinity is observed at mid-flood, when the thickness of the oceanic-water plume reaches the surface.

Averaged over the tidal cycle, the surface salinity field shows a rapid increase in salinity along the channel. Salinity increases from 27 to approximately 31 PSU within a few kilometers of the channel, resulting in a freshwater signal of approximately 31–31.5 PSU across the bay (Figure 3e). The vertical cross-section of salinity shows the formation of a thick freshwater layer that nearly reaches the bottom of the channel, but is surface trapped in the

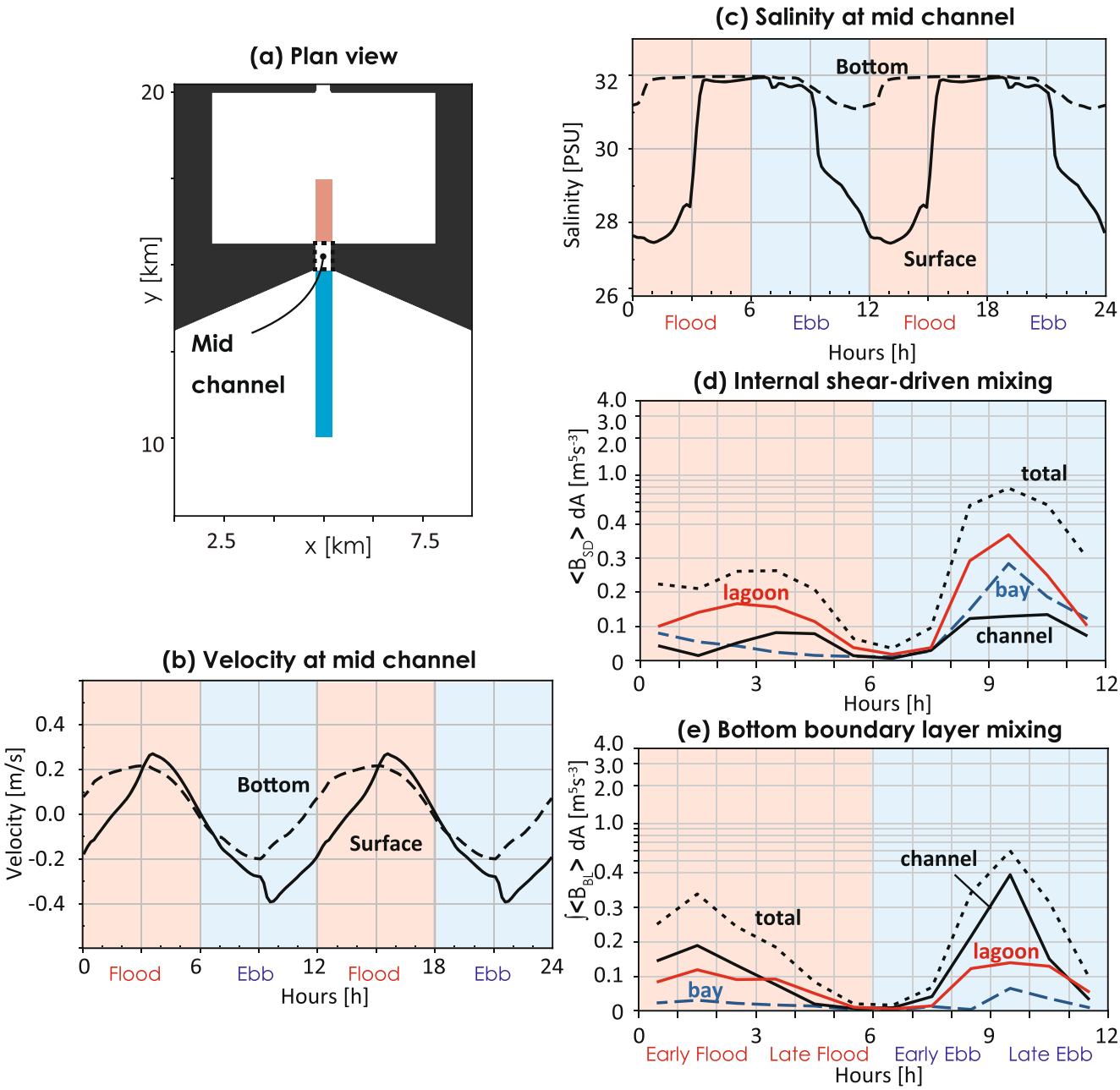

Figure 5. (a) Locations of the mid-channel point and the areas used for estimating area-integrated values for the lagoon, channel, and bay shown as red, dotted, and blue boxes, respectively. (b) Tidal variation in the along-channel velocity and (c) salinity at the mid-channel point for 0.5 m below the surface (solid) and 0.87 m from the bottom (dashed) on day 20 every 10 min. Red and blue shading indicate the flood and ebb tides, respectively. (d) Tidal variation in area-integrated internal shear-driven mixing $\int\langle B_{SD}\rangle dA$ and (e) bottom-boundary-layer mixing $\int\langle B_{BL}\rangle dA$ from hours 0 to 12 on day 20. Red, solid black, dashed blue, and dotted black lines indicate the lagoon, channel, bay, and total values, respectively. Values larger than 0.4 are plotted on a logarithmic scale.

bay. Flow within the channel shows oceanic water intrusion near the bottom and outflow at the height of the freshwater layer, demonstrating the establishment of estuarine circulation. In this study, we define estuarine circulation as a two-layer time-averaged flow, with freshwater outflow near the surface and oceanic water intrusion near the bottom (e.g., MacCready & Geyer, 2010). Comparison with NOTIDES confirms that tides are essential to the establishment of these features. Without tides, the lagoon is occupied by low salinity water from the surface to the bottom and becomes a simple extension of the narrow pathway. A thin freshwater layer with salinity below 27 PSU forms from the channel toward the bay, while the subsurface is quiescent and occupied by oceanic water (Figure 3f). Most of the change in surface salinity occurs in the bay near the surface, and the 29.5 PSU isohaline

is located approximately 5 km from the channel, in contrast to the control experiment, wherein the salinity change begins from the lagoon and the 29.5 PSU isohaline is located in the middle of the channel (Figure 3e).

3.2. Mechanism of Mixing

Low-salinity water and oceanic waters mix through bottom boundary-layer mixing and internal shear-driven mixing. To examine the magnitude of each process, we follow the method of Ralston et al. (2010), partitioning the vertical turbulent buoyancy flux at the depth of the local minimum of turbulent shear stress (d) identified from the vertical profile. Vertical turbulent buoyancy flux and shear stress are estimated to be:

$$B = -g\beta K_Z \frac{\partial S}{\partial z} \tag{3}$$

$$\tau = A_Z \sqrt{\left(\frac{\partial u}{\partial z}\right)^2 + \left(\frac{\partial v}{\partial z}\right)^2} \tag{4}$$

where K_Z and A_Z are estimated from the turbulent closure. The local minimum of τ closest to the bottom is used as d and the magnitude of bottom boundary-layer mixing is estimated through vertical integration of Equation 3 from the bottom (D) to d:

$$\langle B_{BL} \rangle = \int_D^d B dz \tag{5}$$

The magnitude of internal shear-driven mixing is estimated through integration of Equation 3 from d to the sea surface height η:

$$\langle B_{SD} \rangle = \int_d^\eta B dz \tag{6}$$

To examine differences in the mixing mechanism in different areas, $\langle B_{BL} \rangle$ and $\langle B_{SD} \rangle$ are examined from the lagoon to the bay meridionally across the channel (Figure 5a) and away from the influence of the river pathway and the model boundaries. The model results indicate a large difference in τ between the ebb and flood phases (Figures 6a–6d). During the flood phase to early ebb phase, maxima of τ are found at the bottoms of the channel and lagoon. d is located near the surface, reflecting the formation of a thick well-mixed bottom boundary layer. During the late ebb phase, maxima of τ are found at mid-depths in the bay and near the bottoms of the channel and lagoon. This pattern indicates that the freshwater plume is flowing toward the bay and reflects the occurrence of internal shear-driven mixing at its base in the ocean. d is below the middle depths of the channel and lagoon, indicating that the bottom boundary layer is confined to the bottom.

A large difference in B also occurs between the ebb and flood phases (Figures 6e–6h). During the flood phase and early ebb phase, maxima of B are found at mid-depths below depth d, corresponding to the top of the bottom boundary layer. This depth is also the bottom of the thin freshwater plume in the channel. During the late ebb phase, maxima of B are found at mid-depths in the bay and near the bottom of the channel. This pattern aligns with the locations of maxima in τ (Figure 6d) and confirms that the freshwater plume triggers internal shear-driven mixing at its bottom as it enters the bay. The model results suggest that temporal variability in the strength of bottom boundary-layer mixing (Figure 5) is associated with increasing height of the bottom boundary layer from flood to early ebb, when the area near the channel is occupied by a thick oceanic water mass. During late ebb, however, freshwater escapes the shallow areas of the lagoon, creating stratification and triggering mixing. This process results in the formation of a thick freshwater layer and the height of the bottom boundary layer decreases as a result of this thickening. Comparison of τ and B shows that fast tidal flows are forced and generate shear where the bottom slopes, but strong buoyancy flux occurs when stratification coexists during the late ebb.

The time series of $\langle B_{SD} \rangle$ indicates that internal shear-driven mixing is stronger during the ebb phase, when the freshwater plume enters the bay and triggers mixing at its base (Figure 5d). Mixing strengthens first within the lagoon and then in the channel and bay, reflecting the salinity front advecting from the lagoon to the bay. The time series of $\langle B_{BL} \rangle$ also shows that bottom boundary-layer mixing is strengthened twice, reflecting strong currents induced at the mid-ebb and mid-flood stages with a stronger peak occurring in the ebb phase (Figure 5e).

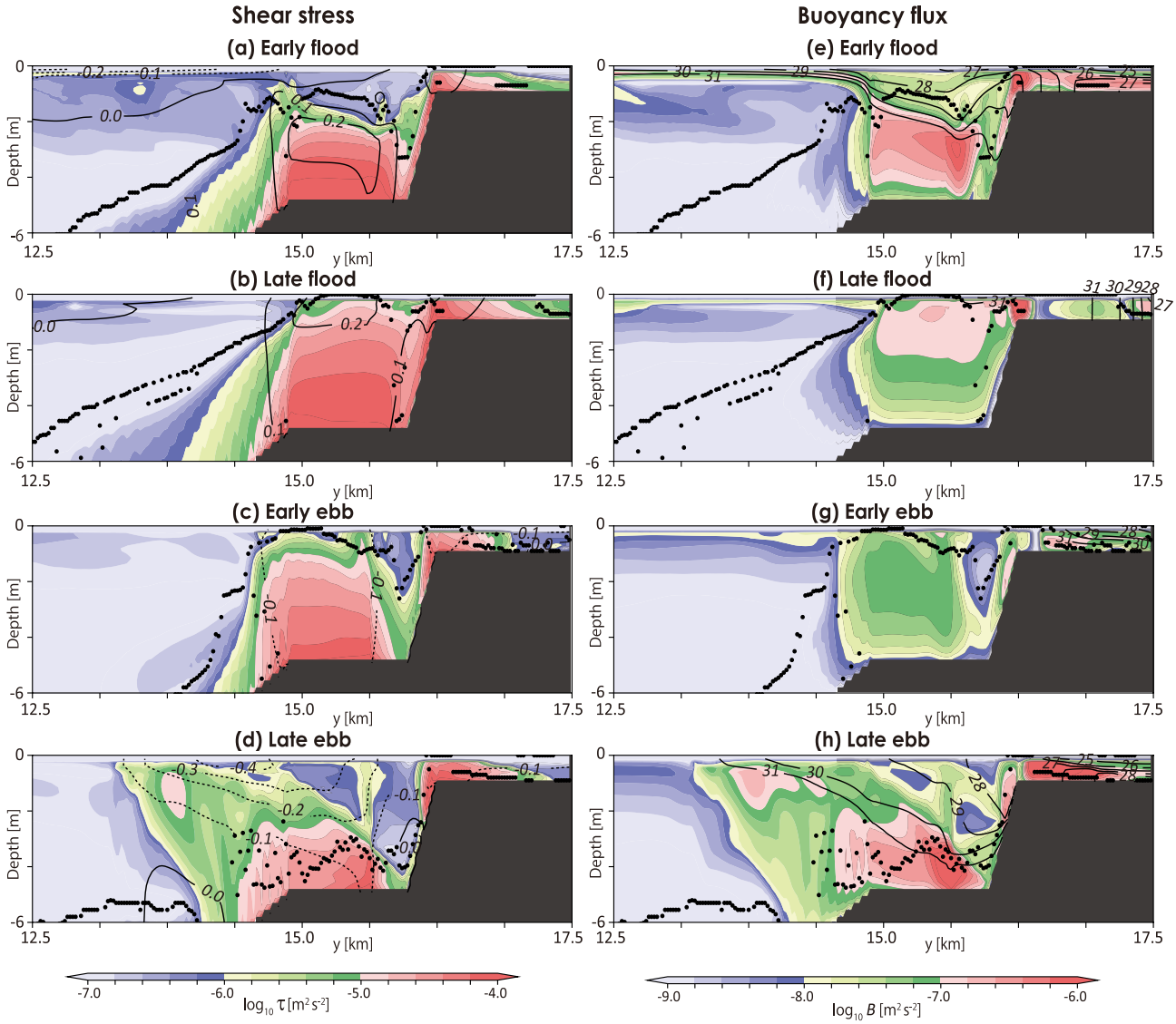

Figure 6. (a) Vertical turbulent shear stresses in the early flood phase (hour 1), (b) late flood phase (hour 4), (c) early ebb phase (hour 7), and (d) late flood phase (hour 10). Estimates are zonal averages across the boxes in Figure 5a. Solid and dashed lines represent northward flow (toward the lagoon) and southward flow (toward the bay), respectively, with a contour interval of 0.1 m s^{-1}. Black dots show the depths of *d*, local minima in vertical turbulent shear stress. Note that the dots do not perfectly align with the minima represented in color due to zonal averaging. (e) Vertical turbulent buoyancy fluxes in the early flood phase (hour 1), (f) late flood phase (hour 4), (g) early ebb phase (hour 7), and (h) late ebb phase (hour 10). Solid lines are isohalines with a contour interval of 1 PSU. Black dots show the depths of *d*, local minima in vertical turbulent shear stress.

3.3. Comparison With Observations

We now compare the model results with observations in the middle of the channel of the Akkeshi Estuary (Figures 2c and 2d). The observations show that the zonal velocity in the channel, which corresponds to along-channel velocity, reverses direction during the tidal cycle both near the surface and near the bottom (Figure 7a). The maximum near-surface flow speed was around 0.4 m s^{-1} during both the flood and ebb phases, while the maximum near-bottom flow speed was about 0.2–0.3 m s^{-1} during the flood phase and below 0.2 m s^{-1} during the ebb phase. These features imply nearly barotropic flow during the flood tide and surface-intensified flow during the ebb tide, resembling the model results that flow toward the lagoon is more barotropic than flow toward the ocean (Figure 5b).

The time series of observed salinity also aligns with the model results. Changes in near-surface salinity lag flow changes by about 6 hr, and near-bottom salinity generally decreases during the late ebb phase (Figure 7b). Salinity

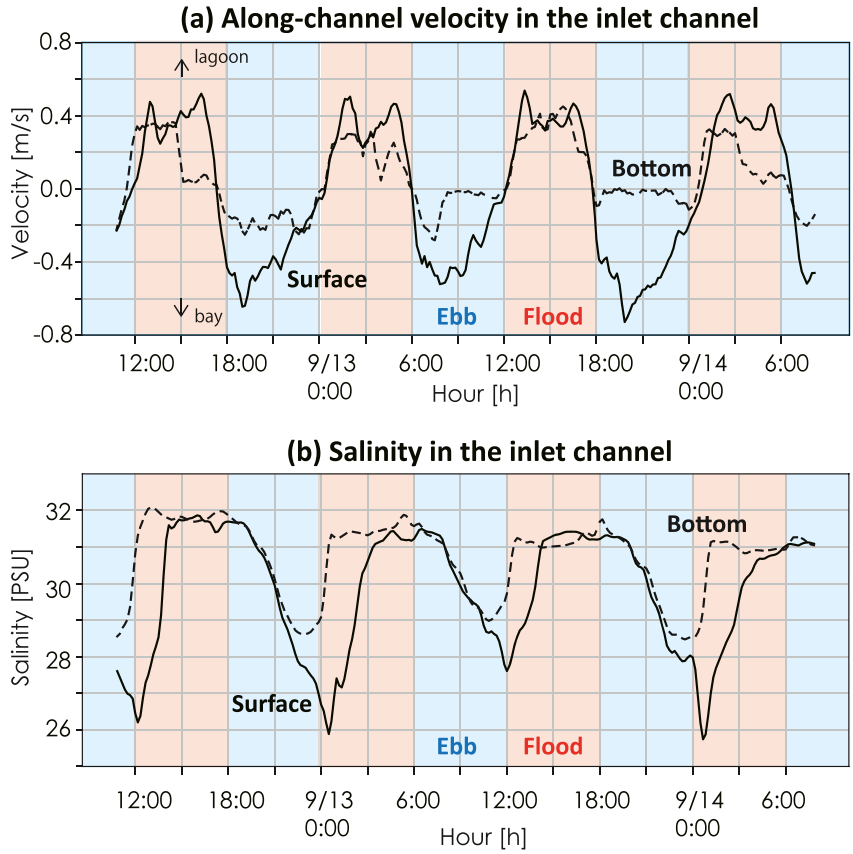

Figure 7. (a) Along-channel velocity and (b) salinity of near-surface (solid black lines) and near-bottom (dashed black lines) waters at the middle of the inlet channel in Akkeshi Bay (Figures 3c and 3d). Positive velocity is toward the lagoon, the same as the model results shown in Figure 5b. Blue and red shading indicate the ebb and flood tides, respectively.

is high, and is the same at the surface and the bottom during the late flood phase, indicating a thick oceanic water column and nearly barotropic flow toward the lagoon (Figure 7a). A decrease in salinity begins in the early ebb phase at both the surface and the bottom; while the bottom salinity quickly returns to high levels at the end of the ebb phase, near-surface salinity abruptly decreases. This feature implies the presence of a sharp salinity front moving from the lagoon to the bay during each tidal cycle. Observations support the formation of tidally generated plumes and the movement of the salinity front found in the model results (Figures 6b and 6c).

4. Sensitivity Experiments

4.1. Depth of the Lagoon

With the depth of the lagoon set to 5 m, equal to the depth of the channel, DEEP shows the formation of a freshwater plume but no oceanic-water plume (Figures 8a–8d). Oceanic water instead intrudes into the lagoon at the subsurface and reaches farther upstream than in the control experiment (Figures 3a–3d). A salinity front is present at the surface, but it remains stagnant near the channel, even in late flood. The freshwater plume near the channel is thin and the extent of mixing is moderate compared to the control experiment (Figures 9a and 9d). Inside the lagoon, the magnitude of bottom boundary-layer mixing is larger during the flood phase than the ebb phase when oceanic water enters the lagoon from the subsurface. The time series of flow and salinity in the channel show that surface and bottom flows change almost simultaneously with the rapid entry of low-salinity water into the ocean after tidal flow reverses from the flood to ebb phase (Figures 8g and 8h). In the absence of an oceanic-water plume, no delay in the salinity time series is found, in contrast to the control experiment (Figures 5b and 5c).

Averaged over the tidal cycle, DEEP shows the establishment of estuarine circulation from the channel to the interior of the lagoon (Figure 8e). In the control experiment, such two-layer circulation formed in the channel

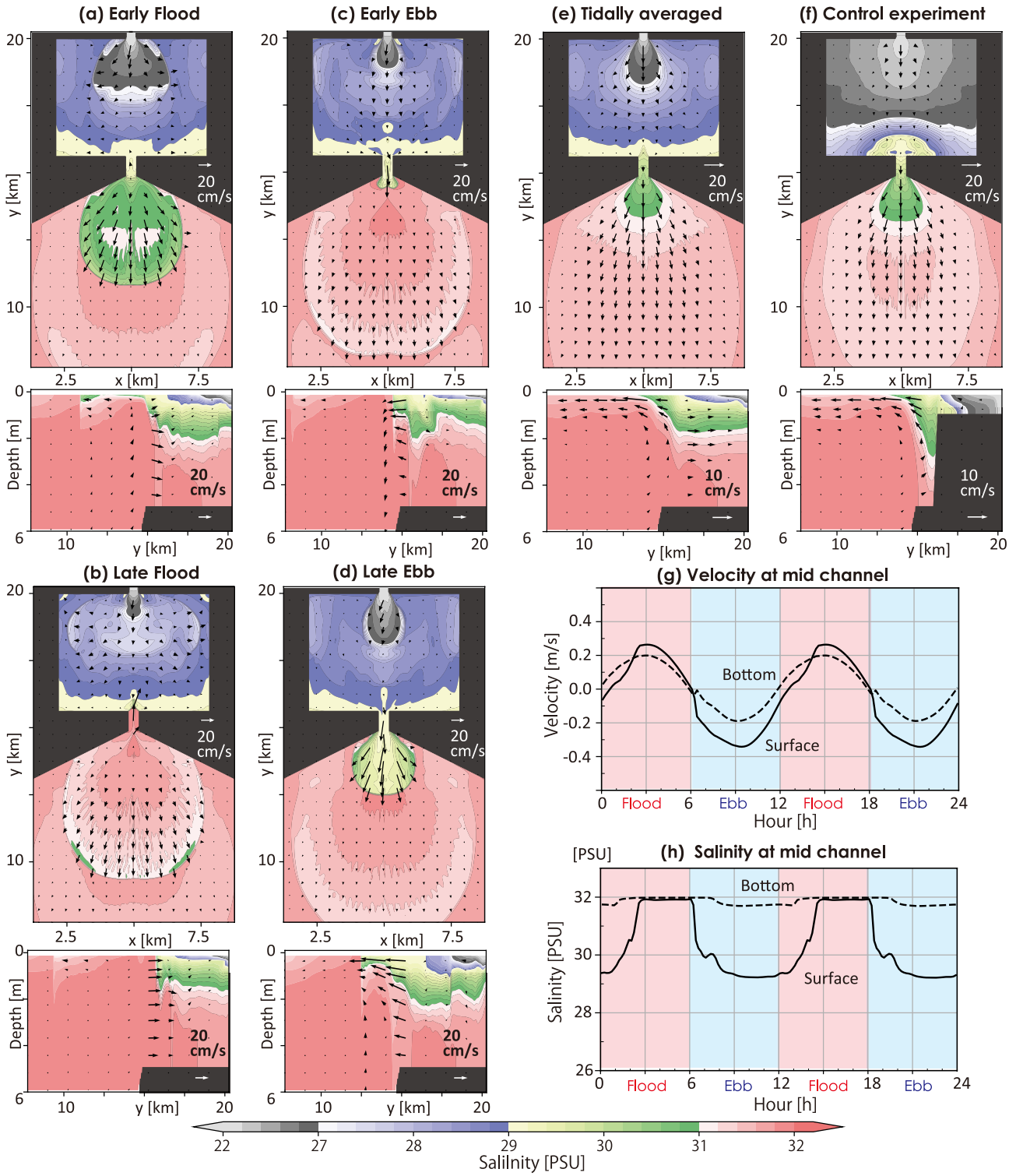

Figure 8. (a) Surface flow and salinity fields for DEEP in the early flood phase (hour 1), (b) the late flood phase (hour 4), (c) the early ebb phase (hour 7), (d) the late ebb phase (hour 10), and (e) tidally averaged, and for (f) the tidal average of the control experiment. The upper panels represent the surface within the white dashed box in Figure 2a and the lower panels show a vertical cross-section along the black dotted line within the box. (g) Time series of along-channel velocity and (h) salinity at the mid-channel point at 0.5 m below the surface (solid line) and 0.87 m from the bottom (dashed line) on day 20 every 10 min. Red and blue shading indicate the flood and ebb tides, respectively.

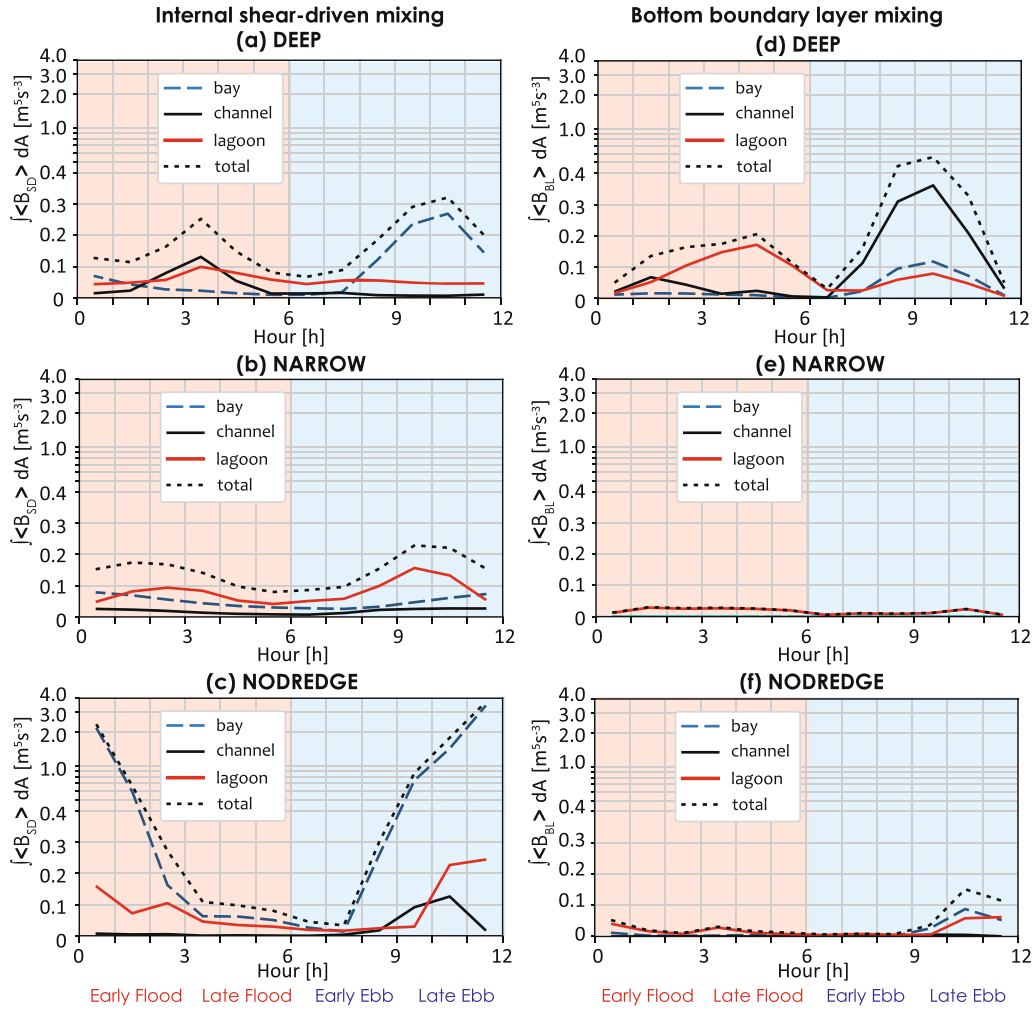

Figure 9. (a) Time series of area-integrated internal shear-driven mixing $\int\langle B_{SD}\rangle dA$ from hours 0 to 12 on day 20 for DEEP, (b) NARROW, and (c) NODREDGE. Red, solid black, dashed blue, and dotted black lines indicate the lagoon, channel, bay, and total values, respectively. (d) Time series of area-integrated bottom boundary-layer mixing $\int\langle B_{BL}\rangle dA$ from hours 0 to 12 on day 20 for DEEP, (e) NARROW, and (f) NODREDGE. Values larger than 0.4 are plotted on a logarithmic scale.

and the sloping part of the lagoon, but not in the shallow part of the lagoon (Figure 8f). Therefore, DEEP indicates that one role of the shallow lagoon is to generate a barotropic oceanic-water plume within the shallow area rather than subsurface oceanic water intrusion. On the oceanic side, a freshwater plume develops with higher salinity than in the control experiment. Mixing near the channel becomes moderate in DEEP, especially for the ebb phase (Figures 9a and 9b), and the surface water of the lagoon is saltier due to mixing with oceanic water at the subsurface.

4.2. Depth of the Inlet Channel

With the depth of the channel remaining shallow, NODREDGE shows the formation of a freshwater plume and an oceanic-water plume that are vertically well mixed in the channel (Figures 10a–10d). Bottom boundary-layer mixing decreases because stratification is absent and the freshwater plume remains fresh, prohibited from thickening beyond the channel depth. Strong mixing is induced when the freshwater plume enters the ocean during the ebb phase. The maximum flow speed is approximately 0.7 m s^{-1} (Figure 10c), which is much faster than in the control experiment (0.2 m s^{-1}) (Figure 5b), and salty oceanic water is present below the region where the freshwater enters the ocean. As a result, vertical shear increases, inducing abrupt and much stronger mixing than observed in the control or DEEP experiments. The occurrence of this intense mixing is apparent as strong upwelling on the

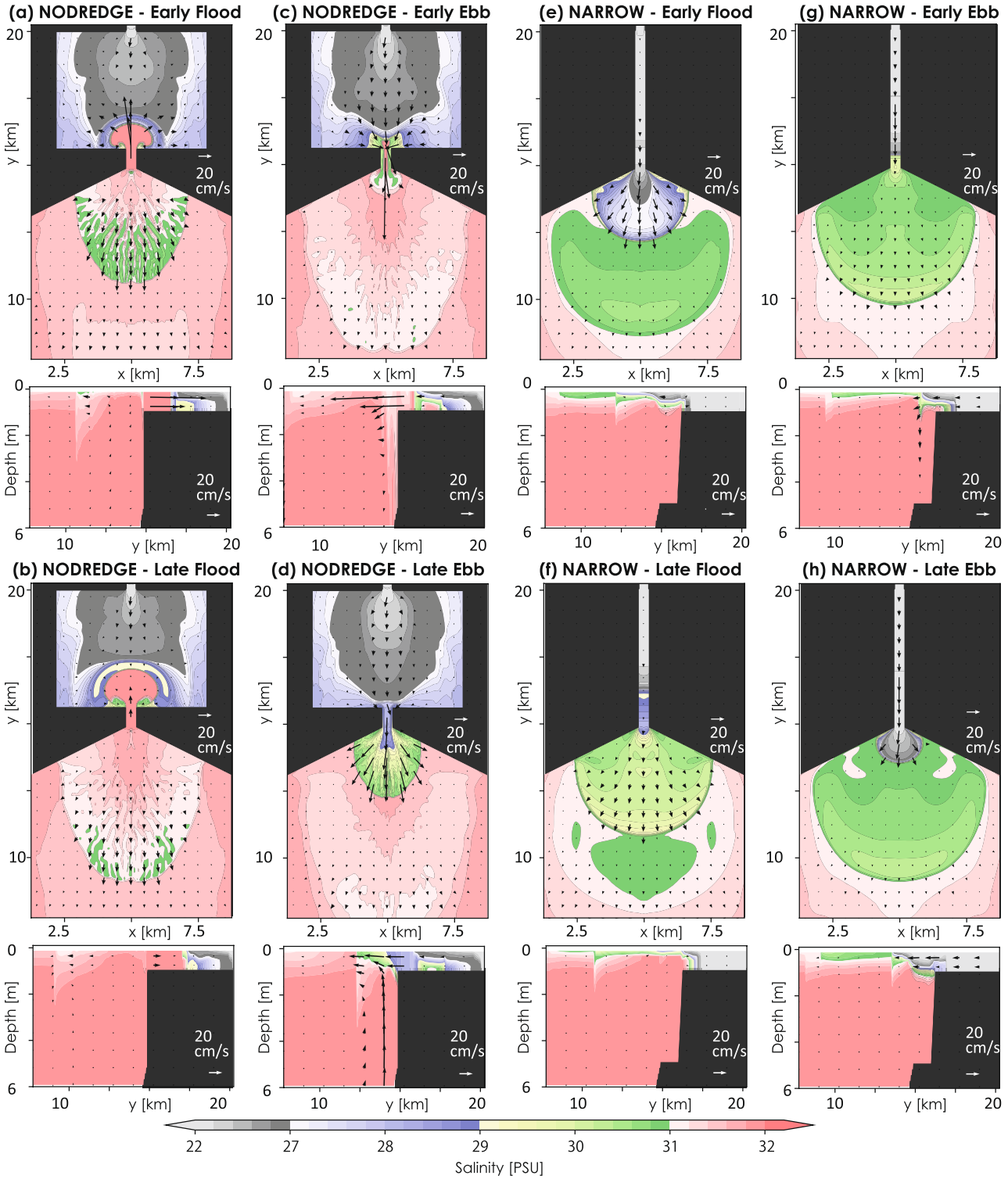

Figure 10. Surface flow and salinity fields during the (a) early flood (hour 4), (b) late flood (hour 7), (c), early ebb (hour 10), and (d) late ebb (hour 1) phases in NODREDGE. Surface flow and salinity fields during the (e) early flood (hour 1), (f) late flood (hour 4), (g), early ebb (hour 7), and (h) late ebb (hour 10) phases in NARROW. The upper panel represents the surface within the white dashed box in Figure 2a and the lower panel shows a vertical cross-section along the black dotted line within the box.

oceanic side of the channel. Once in the ocean, the freshwater plume disperses as in the control experiment. The oceanic-water plume enters the lagoon as a barotropic and vertically well-mixed flow, which remains salty and creates a sharp salinity front inside the lagoon. NODREDGE confirms that shallow depth within the lagoon is responsible for the formation of the salinity front in the control experiment (Figures 3b and 3c).

NODREDGE indicates that the increase in depth from the lagoon to the channel in the control experiment enables formation of a thick, baroclinic freshwater plume in the channel. In NODREDGE, the velocity of the freshwater plume is approximately 0.2 m s^{-1} during the ebb phase on average, and around 1 hr is required for the plume to cross the channel from the lagoon to the ocean. This time is ample for bottom boundary-layer mixing to fully mix the water column vertically within the channel. Scaling shows that the time necessary for mixing $\left(\frac{H^2}{A_Z}\right)$ is about 20 min based on the depth of 1 m and the turbulent vertical diffusivity of 10^{-3} m^2 s^{-1} simulated in the model. However, at a channel depth of 5 m, as in the control experiment, mixing requires about 7 hr; in that case, the freshwater plume can become thick within the channel but not thick enough to eliminate baroclinicity of the water column. Similarly, one can evaluate the F_r-M space of Geyer and MacCready (2014), where F_r is the Froude number $(\frac{u}{\sqrt{g'H}})$, M is a parameter comparing the mixing and tidal time scales, and g' is the reduced gravity (here we use the salinity difference between the river flow and oceanic water). Based on the flow speed induced by the river flow v_r for u, M and F_r are approximately 1.6 and 0.16 in NODREDGE (0.14 m s^{-1} is used for tidal flow speed), indicating either a well-mixed condition or time-dependent salt wedge. For DEEP, M and F_r are approximately 0.5 and 0.014, suggesting a partially mixed or stratified condition. These conditions align well with the model results.

4.3. Lagoon Size and the Salinity Balance

Equation 2 indicates that the area of the lagoon (A) affects the dynamics of freshwater outflow. For NARROW, A is at its minimum, and v_c is 0.02 m s^{-1}, comparable to v_r, the flow induced by river flow. The model results show that near-surface flow in the channel is primarily toward the ocean (Figures 10e–10h); compared to the control experiment (Figure 3a), the freshwater plume is thinner and fresher. Intrusion of oceanic water occurs only during the late flood phase and within a small distance of the river mouth. Mixing is weak throughout the tidal cycle (Figures 9b and 9e). Again, the shift to a more baroclinic flow in NARROW from a more barotropic flow simulated in the control experiment can be explained by the difference in Froude number due to the tidal flow speed using v_c. Fr is near zero in the channel for NARROW, but 0.44 for the control experiment. Therefore, mixing is likely to be more limited in NARROW and make the flow baroclinic.

The impact of tidal flow speed at the channel on the mass and freshwater balance can be examined using the estuarine Richardson number (e.g., Nash et al., 2009), $Ri_E = \frac{g'Q}{W u_{tidal}^3}$, which compares the magnitude of turbulence to advective fluxes. In this study, v_c is used for u_{tidal}. Ri_E decreases as A increases, and the tidally averaged salinity of the freshwater plume in the channel increases accordingly (Figure 11a). Salinity is averaged across the channel at the mid-channel point, and the freshwater plume is defined here as the southward flow component, which tends to occur in the upper part of the water column. Oceanic flow is defined as the opposite flow component, which tends to occur in the lower part of the water column. The increase in the salinity of the freshwater plume implies enhanced mixing, in accordance with the tidally driven increase in turbulent flux through changes in A or the tidal elevation, as Equation 2 indicates. Note that Ri_E can also be expressed as the ratio of the channel volume to the volume increase within the lagoon caused by tides, R_{LC}:

$$Ri_E = \frac{g'Q}{W v_c^3} = \frac{g'QT^3}{64W}\left(\frac{H \cdot W \cdot L}{A \cdot \Delta\eta}\right)^3 = \frac{g'QT^3}{64W} {R_{LC}}^{-3}$$

where L is the channel length. Thus, a decrease in Ri_E indicates an increase R_{LC}, leading to an increase in lagoon size relative to channel size (Figure 11c).

Sensitivity experiments further demonstrate that the time-averaged transport of the freshwater plume in the channel (U) peaks when Ri_E is approximately unity. Here, U is defined as the transport of the southward flow component across the channel. For Ri_E above one, U increases with decreasing Ri_E (Figure 11a). This result is consistent with the increase in salinity of the freshwater plume as Ri_E decreases. As more oceanic water is entrained into the freshwater plume, U increases, and estuarine circulation is enhanced.

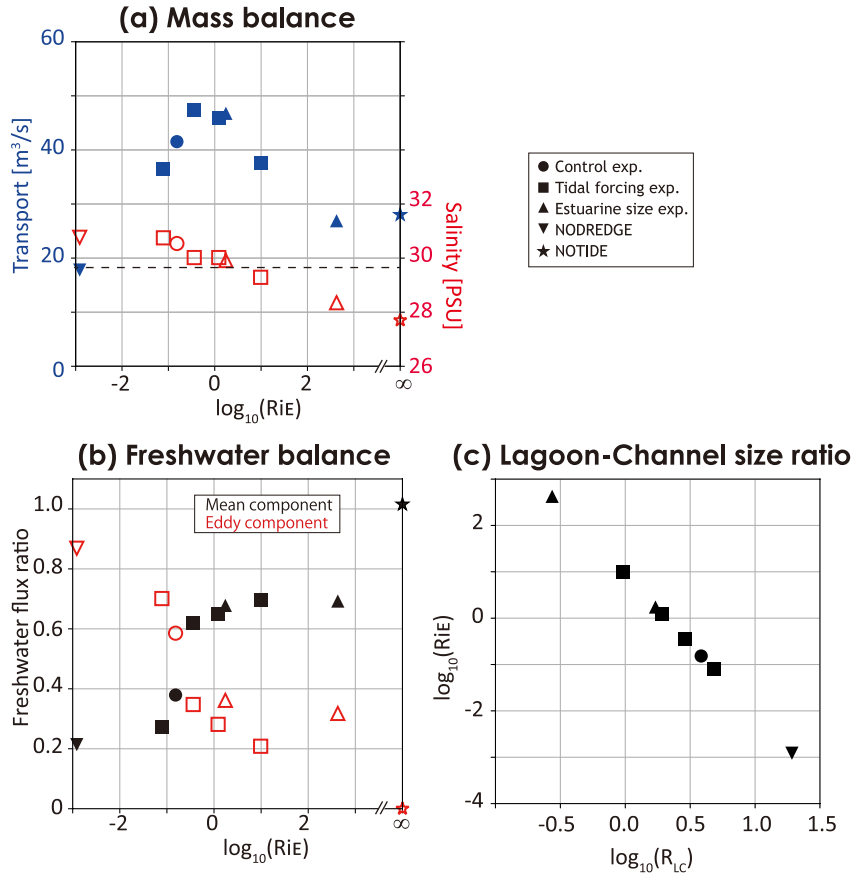

Figure 11. (a) Sensitivity of freshwater transport (filled blue symbols) and salinity (open red symbols) in the channel to Ri_E, the estuarine Richardson number. The dashed line is the river discharge rate. Circles, squares, up- and down-pointed triangles, and stars indicate data from the control, tidal forcing, lagoon area, NODREDGE, and NOTIDE experiments, respectively. (b) Sensitivity values of the time-average flow component (filled black symbols) and eddy component (open red symbols) to Ri_E. Each component is shown as a ratio to total freshwater flux (=180 PSU m^3 s^{-1}). (c) Relationship between R_{LC} ($=\frac{A\Delta\eta}{WLD}$) and Ri_E.

For Ri_E below one, as in the control experiment, U tends to decrease as Ri_E decreases (Figure 11a). This trend arises because tidal pumping, which is the time-varying component of exchange flow in the channel, begins to replace part of the water mass and freshwater exchange induced by the estuarine circulation rather than simply enhancing estuarine circulation. The increasing role of tidal pumping is clear when examining the freshwater balance across the channel. We define freshwater flux as $U(S_0 - S)$, where S_0 is the reference salinity, 32 PSU (i.e., the oceanic value), and the freshwater flux due to the river flow is 180 PSU m^3 s^{-1}. Flow through the channel must balance this flux for the salinity of the lagoon to achieve steady state. To compare the roles of the time-averaged flow and time-varying flow, we partition the freshwater flux into time-averaged and eddy components:

$$\overline{U(S_0 - S)} = \overline{U}\left(S_0 - \overline{S}\right) - \overline{U'S'} \tag{7}$$

where variables with overbars are temporal averages over the tidal cycle and variables with prime symbols are residuals. The first term on the RHS of Equation 7 represents freshwater flux due to river inflow and estuarine circulation, which tends to occur as two-layer flow. The second term represents freshwater flux due to tidal pumping.

Sensitivity experiments show that as Ri_E decreases, the role of tidal pumping in driving freshwater flux increases, assuming a greater role than that of estuarine circulation when Ri_E is less than one, as in the control experiment (Figure 11b). At $Ri_E \sim 1$, both tidal pumping and estuarine circulation are large and augment each other, thus maximizing mean transport. For $Ri_E > 1$, advective flux is stronger and thus estuarine circulation is dominant,

whereas for $Ri_E < 1$, turbulent flux induced by tides is stronger, flow across the channel becomes more barotropic, and tidal pumping becomes dominant.

4.4. Role of the Coriolis Force

The Coriolis force causes geostrophic adjustment and the freshwater plume becomes a coastal current, even for small-scale rivers (e.g., Lemagie & Lerczak, 2020). Accordingly, our results show more low-salinity water trapped along the western half of the bay in CORI than in the control experiment (Figures 12a–12d). A coastal current is established with weak anticyclonic circulation, similar to the simulation results for a mid-scale river reported by Wheless and Valle-Levinson (1996). By contrast, near the channel, tides still generate freshwater and oceanic-water plumes. The apparent weak impact of the Coriolis force on tidal pumping arises because the time scale of these flows is less than a day (i.e., 12 hr).

4.5. Impact of Spatial Scale

The behavior of the freshwater exchange changes significantly when the spatial scale of the model domain is large and the river discharge rate is high. LARGE shows stable salinity stratification in the channel and flow that oscillates with the tidal cycle (Figures 12e–12h). Outside the channel, anticyclonic circulation and a coastal current are present. As the spatial scale is large, the flow is primarily governed by geostrophy; the width of the channel (4 km) and the deformation radius of about 3 km lead to a Kelvin number greater than 1. Within the lagoon, the water mass becomes fresher because the intrusion of oceanic water does not reach shallow regions of the lagoon; for a large lagoon, there is ample time for uniform vertical mixing of the water mass.

5. Discussion

The geometric characteristics of a lagoon, such as lateral constriction and depth, affect the dynamics and mixing of freshwater exchange across an inlet channel. A large semi-enclosed lagoon is found to create strong tidal flows in the channel, which enhances mixing from flow convergence and acceleration when the salinity front is advected toward the ocean. DEEP shows this process clearly, as bottom boundary-layer mixing strengthens in the channel much more than in the lagoon during the ebb phase (Figure 9a). The only difference between the channel and lagoon in DEEP is the zonal length, implying that the lateral constriction is responsible for the enhanced mixing. For the control experiment, internal shear-driven mixing also occurs where the thicker freshwater layer shoals inside the channel. To further examine the role of lateral constriction, we conducted an experiment in which the lagoon is a straight channel with the same total area (A) as the control experiment by making it narrow and approximately 60 km long (Figure S1). The impact of channel meanders on tidal flow is minor. If the strength of the tidal flow remains constant, the experiment should show the role of lagoon geometry in freshwater exchange. However, the experiment shows weak tidally reversing flow, and greatly reduced salinity of the outflow. Enhanced bottom boundary-layer mixing no longer occurs in the channel. Although A is similar, the strength of the tidal flow decreases when the lagoon becomes an extremely long channel because the surface gravity wave speed ($\sqrt{gH}$) is about 3 m s^{-1}, meaning waves can travel only about 10 km per hour, which is not fast enough to cause a simultaneous response throughout the long estuary. This condition is dynamically similar to a reduction of A in Equation 2. For small-scale river flows, the lagoon is often a few kilometers in length; therefore, a difference in the width scale between the channel and lagoon is likely to coexist that may enhance mixing through the formation of oceanic-water plumes and fronts. Such mixing is the key factor associated with changes in A, as examined in the lagoon area experiment (Table 1).

The magnitude of estuarine circulation, estimated as the time-averaged transport of freshwater across the channel, is about 42, 29, and 19 m^3 s^{-1} in the control experiment, DEEP, and NODREDGE, respectively. For NODREDGE, this exchange transport is nearly identical to the transport of river flow, as estuarine circulation is absent. The theoretical estimate of estuarine circulation is $v_e = \frac{g\beta D^3}{48K_Z}\frac{\partial S}{\partial y}$ (Hansen & Rattray, 1965), where D is the depth of the river and y is the direction along the river pathway, which indicates an increase in strength with greater depth and explains the increase from NODREDGE to DEEP. However, in the control experiment, the lagoon is generally 1 m deep, similar to NODREDGE, but the circulation is stronger than that in DEEP,

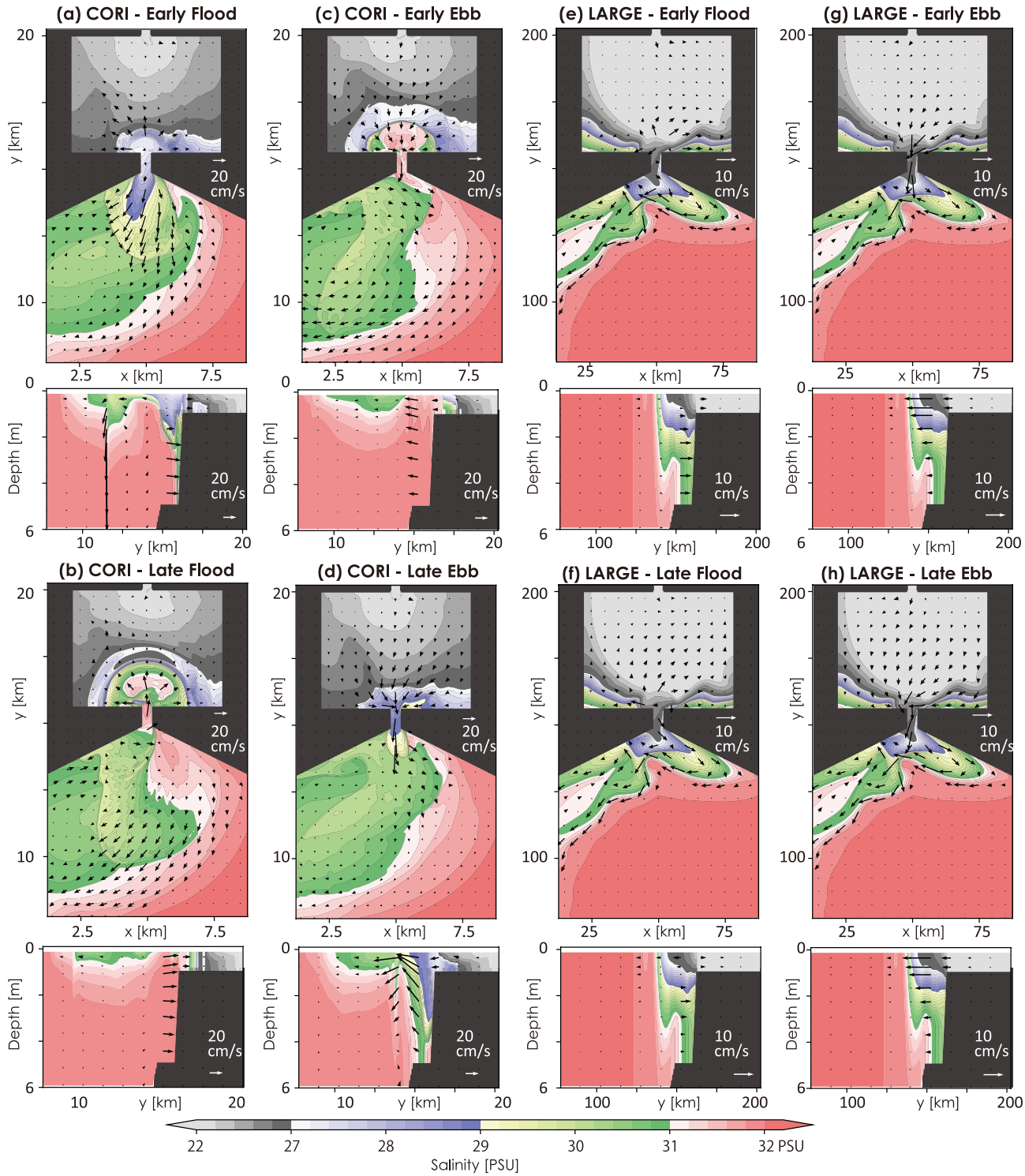

Figure 12. Surface flow and salinity fields during the (a) early flood (hour 1), (b) late flood (hour 4), (c) early ebb (hour 7), and (d) late ebb (hour 10) phases for CORI. Surface flow and salinity fields during the (e) early flood (hour 6), (f) late flood (hour 9), (g) early ebb (hour 0), and (f) late ebb (hour 3) phases on day 201 for LARGE. The upper panel represents the surface within the white dashed box in Figure 2a and the lower panel shows a vertical cross-section along the black dotted line within the box.

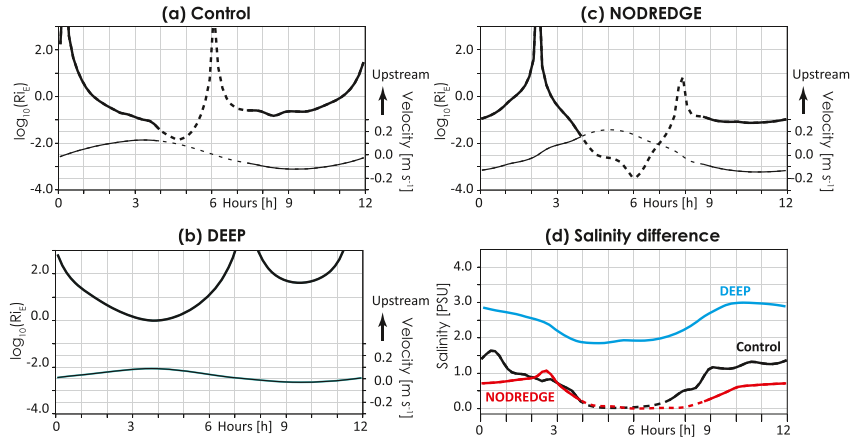

Figure 13. Time series of the estuarine Richardson number (Ri_E) (thick line) and vertically averaged velocity (thin line) in the lagoon area shown in Figure 5a from hours 0 to 12 on day 20 in the (a) control, (b) DEEP, and (c) NODREDGE experiments. (d) Salinity difference between the surface and bottom for control (black), DEEP (blue), and NODREDGE (red). Dashed lines indicate salinity differences of less than 0.1 PSU between the surface and bottom.

which is the opposite of the result expected from the change in depth. We find that this enhancement of estuarine circulation is a result of mixing induced by tidal flows forced across the slope and the asymmetry of the stratification created across a sloping bottom within the lagoon. As the estimates of Fr (or M) in Section 4.2 indicate, a vertically well-mixed water column is expected for a depth of 1 m, but not for 5 m, so the shallow area of the lagoon becomes non-stratified while that close to the channel is stratified. Tidal flows are also fast in shallow areas. Thus, as the salinity front moves toward the ocean during the late ebb, a freshwater plume exits the shallow area, interacts with the subsurface oceanic water, and induces intense internal shear-driven and bottom boundary-layer mixing as the plume thickens, then moves toward deeper water and reaches the channel (Figures 5d and 5e). The bottom interface of the thick freshwater layer then shoals in the ocean and induces internal shear-driven mixing. Strong mixing would occur in NODREDGE within the lagoon, where the flow is fast and Ri_E is low, but is prohibited by the lack of both stratification and oceanic water for mixing below the freshwater for approximately half of the tidal cycle (Figure 13c). Thus, intense mixing driven only by internal shear occurs after the freshwater enters the ocean (Figures 9c and 9d). This difference results in enhanced estuarine circulation in the control experiment along with strong upwelling in the sloping area, but not in NODREDGE. Compared to DEEP, the magnitude of the buoyancy flux created within the lagoon over the tidal cycle is approximately 1.7 times larger in the control experiment (Figures 5d, 5e, and 9a, 9b), confirming the presence of enhanced mixing. Furthermore, we find that bottom boundary-layer mixing comprises about 33% of the total mixing. As Spicer et al. (2021) found for tidal pulsed plumes on the oceanic slope, we find that bottom boundary-layer mixing plays a role equally important to that of internal shear-driven mixing.

The importance of the salinity front to mixing within the lagoon is reflected in the primary mixing phase. In DEEP, stronger mixing occurs when oceanic water intrudes during the flood rather than the ebb phase (Figures 9a and 9d). Stratification is present throughout the tidal cycle and the Ri_E, estimated using the vertically averaged flow speed for u_{tidal} and the salinity difference between the surface and bottom within the lagoon for g', is lower during the flood phase (Figure 13b) and weakens stratification (Figure 13d). In the control experiment, Ri_E decreases during the late flood phase (Figure 13a); however, the turbulent flux becomes ineffective at mixing the water column (Figure 13d) because stratification is very weak when the salinity front forms and moves upstream. Active mixing returns when stratification is re-established in the early ebb phase. Thus, the magnitude of Ri_E and the period of active mixing during the flood and ebb phases are similar (Figure 4e). In NODREDGE, a salinity front quickly forms, and stratification is very weak, making turbulent flux ineffective during much of the flood period (Figure 13d); thus, the ebb phase is the primary mixing phase in NODREDGE (Figures 9c, 9f, and 13c). The importance of mixing during the ebb phase is similar to that found for a salt wedge for mid-size rivers and a deeper estuarine basin (Ralston et al., 2010). In a shallower environment with small discharge, internal shear-driven and bottom boundary mixing occur more simultaneously, rather than internal shear-driven mixing occurring in advance (Figures 5d and 5e).

The length of the inlet channel was constant in our study, but varies among estuaries. As a longer channel limits lateral dispersion of the freshwater plume, we suspect that more mixing will occur within the channel, thickening the freshwater plume compared to that from short channels. Another important bathymetric feature is the location of the slope inside the lagoon and the steepness of the slope along the rim of the bay. If the slope inside the lagoon is located far from the channel, the exchange flow will become more like DEEP. A steeper slope along the rim of the bay may not directly affect freshwater exchange flow, as the lift-off point is located within the channel in our model. However, a steep oceanic slope may affect processes that were neglected in this study, such as oceanic currents and waves, and thereby affect freshwater outflow.

6. Conclusion

This study investigates the impact of a large shallow lagoon on the dynamics of freshwater exchange across a deep inlet channel, focusing on lagoons affected by river flow with a small discharge rate. Idealized numerical model experiments show that large lagoons with narrow inlets induce tidal pumping, generating a stratified freshwater plume in the ocean and a vertically well-mixed oceanic-water plume within the lagoon. Strong tidal pumping and estuarine circulation enhance freshwater export from the lagoon to the ocean when the estuarine Richardson number is approximately one. Below one, tidal pumping becomes dominant while above one, estuarine circulation becomes more important. In the presence of a deep inlet channel, tidal flows enhance mixing and estuarine circulation for shallow than deep lagoons, attributable to the asymmetric stratification associated with the sloping bottom. A shallow lagoon makes the oceanic water intrusion barotropic, resulting in the formation of a sharp salinity front inside the lagoon. This salinity front then moves from the lagoon to the ocean, playing a key role in driving mixing and exchange flow. Because fast tidal flows are forced by shallow depth, strong internal shear-driven and bottom boundary-layer mixing develops as the front exits the shallow area, moves toward deeper water, and encounters oceanic water below. Lateral constriction further enhances mixing through convergence and acceleration.

To focus on the basic dynamics of riverine and oceanic waters, we neglected the role of atmospheric forcing in this manuscript. Winds can enhance vertical mixing near the surface and drive surface flows both locally and remotely, and their strength varies on multiple time scales. The magnitude and patterns of vertical mixing are also affected by waves and surface heat fluxes. Enhanced background vertical mixing is likely to cause more vertically diffused freshwater outflow into the ocean and fresher estuarine water, as mixing in a shallow system prohibits the intrusion of oceanic water. We suspect that weather events also create spatial variation in water-mass properties within the estuary, as approximately 2 weeks is needed to spin up the model; assessing this possibility is a subject for future research. As the strength and direction of winds are likely to change seasonally, regional variation should be thoroughly examined using a model with realistic bathymetry and coastlines.

Data Availability Statement

The processed observational data is available on Figshare (Kida et al., 2022). Weather station data was obtained from Japan Meteorological Agency website (Japan Meteorological Agency, 2023). The numerical model code for KINACO is available at Matsumura (2023) and the input files for the numerical model experiments are available on GitHub, https://github.com/shinkida/Akkeshi_Circulation (Kida, 2023). Figures were made with Matplotlib version 3.7.0 (Hunter, 2007), available under the Matplotlib license at https://matplotlib.org.

Acknowledgments
The authors thank S. Hamano and H. Katsuragawa for their assistance during the field measurements and anonymous reviewers for many insightful comments. This work was supported by JSPS KAKENHI Grants JP21H03591 and JP23H04821 and the Joint Research Program of the Institute of Low-temperature Science, Hokkaido University.

References

Basdurak, N. B., Largier, J. L., & Nidzieko, N. J. (2020). Modeling the dynamics of small-scale river and creek plumes in tidal waters. *Journal of Geophysical Research*, *125*(7), e2019JC015737. https://doi.org/10.1029/2019JC015737

Bauer, J. E., Cai, W. J., Raymond, P. A., Bianchi, T. S., Hopkinson, C. S., & Regnier, P. A. (2013). The changing carbon cycle of the coastal ocean. *Nature*, *504*(7478), 61–70. https://doi.org/10.1038/nature12857

Carmack, E., Winsor, P., & Williams, W. (2015). The contiguous panarctic riverine coastal domain: A unifying concept. *Progress in Oceanography*, *139*, 13–23. https://doi.org/10.1016/j.pocean.2020.102455

Chen, S. N., Geyer, W. R., Ralston, D. K., & Lerczak, J. A. (2012). Estuarine exchange flow quantified with isohaline coordinates: Contrasting long and short estuaries. *Journal of Physical Oceanography*, *42*(5), 748–763. https://doi.org/10.1175/jpo-d-11-086.1

Ding, M. (2020). *An analysis of hydrological characteristics in the tidal zone of Bekanbeushi river basin, Master's thesis*. Graduate School of Environmental Science Hokkaido University.

Garvine, R. W. (1995). A dynamical system for classifying buoyant coastal discharges. *Continental Shelf Research*, *15*(13), 1585–1596. https://doi.org/10.1016/0278-4343(94)00065-u

Geyer, W. R., & MacCready, P. (2014). The estuarine circulation. *Annual Review of Fluid Mechanics*, *46*(1), 175–197. https://doi.org/10.1146/annurev-fluid-010313-141302

Hansen, D. V., & Rattray, M. (1965). Gravitational circulation in straits and estuaries. *Journal of Marine Research*, *23*, 104–122.

Hench, J. L., Blanton, B. O., & Luettich, R. A., Jr. (2002). Lateral dynamic analysis and classification of barotropic tidal inlets. *Continental Shelf Research*, *22*(18–19), 2615–2631. https://doi.org/10.1016/s0278-4343(02)00117-6

Hench, J. L., & Luettich, R. A. (2003). Transient tidal circulation and momentum balances at a shallow inlet. *Journal of Physical Oceanography*, *33*(4), 913–932. https://doi.org/10.1175/1520-0485(2003)33<913:ttcamb>2.0.co;2

Hunter, J. D. (2007). Matplotlib: A 2D graphics environment. *Computing in Science & Engineering*, *9*(3), 90–95. https://doi.org/10.1109/mcse.2007.55

Isada, T., Abe, H., Kasai, H., & Nakaoka, M. (2021). Dynamics of nutrients and colored dissolved organic matter absorption in a wetland-influenced subarctic coastal region of northeastern Japan: Contributions from mariculture and eelgrass meadows. *Frontiers in Marine Science*, *1452*. https://doi.org/10.3389/fmars.2021.711832

Isada, T., Hooker, S. B., Taniuchi, Y., & Suzuki, K. (2022). Evaluation of retrieving chlorophyll a concentration and colored dissolved organic matter absorption from satellite ocean color remote sensing in the coastal waters of Hokkaido, Japan. *Journal of Oceanography*, *78*(4), 1–14. https://doi.org/10.1007/s10872-022-00633-w

Iwanaka, Y., & Isobe, A. (2018). Tidally induced instability processes suppressing river plume spread in a nonrotating and nonhydrostatic regime. *Journal of Geophysical Research*, *123*(5), 3545–3562. https://doi.org/10.1029/2017JC013495

Izett, J. G., & Fennel, K. (2018). Estimating the cross-shelf export of riverine materials: Part 2. Estimates of global freshwater and nutrient export. *Global Biogeochemical Cycles*, *32*, 176–186. https://doi.org/10.1002/2017GB005668

Japan Meteorological Agency. (2023). Automated meteorological data acquisition system (AMeDAS) [Dataset]. JMA. Retrieved from https://www.data.jma.go.jp/risk/obsdl/index.php

Kapolnai, A., Werner, F. E., & Blanton, J. O. (1996). Circulation, mixing, and exchange processes in the vicinity of tidal inlets: A numerical study. *Journal of Geophysical Research*, *101*(C6), 14253–14268. https://doi.org/10.1029/96jc00890

Kida, S. (2023). Model configuration files of KINACO used for Akkeshi Circulation experiments [Software]. Zenodo. https://doi.org/10.5281/zenodo.8361476

Kida, S., Tanaka, K., Isada, T., & Nakamura, T. (2022). Oceanographic data collected in September 2018 in Akkeshi Bay [Dataset]. Figshare. https://doi.org/10.6084/m9.figshare.20342091

Kilcher, L. F., & Nash, J. D. (2010). Structure and dynamics of the Columbia River tidal plume front. *Journal of Geophysical Research*, *115*(C5), C05S90. https://doi.org/10.1029/2009jc006066

Lemagie, E., & Lerczak, J. (2020). The evolution of a buoyant river plume in response to a pulse of high discharge from a small midlatitude river. *Journal of Physical Oceanography*, *50*(7), 1915–1935. https://doi.org/10.1175/JPO-D-19-0127.1

Luketina, D. A., & Imberger, J. (1987). Characteristics of a surface buoyant jet. *Journal of Geophysical Research*, *92*(C5), 5435–5447.

MacCready, P. (2004). Toward a unified theory of tidally-averaged estuarine salinity structure. *Estuaries*, *27*(4), 561–570. https://doi.org/10.1007/bf02907644

MacCready, P., & Geyer, W. R. (2010). Advances in estuarine physics. *Annual Review of Marine Science*, *2*(1), 35–58. https://doi.org/10.1146/annurev-marine-120308-081015

Matsumura, Y. (2023). KINACO source code [Software]. AORI. http://lmr.aori.u-tokyo.ac.jp/feog/ymatsu/kinaco.git/

Matsumura, Y., & Hasumi, H. (2008). A non-hydrostatic ocean model with a scalable multigrid Poisson solver. *Ocean Modelling*, *24*(1–2), 15–28. https://doi.org/10.1016/j.ocemod.2008.05.001

McPherson, R. A., Stevens, C. L., O'Callaghan, J. M., Lucas, A. J., & Nash, J. D. (2020). The role of turbulence and internal waves in the structure and evolution of a near-field river plume. *Ocean Science*, *16*(4), 799–815. https://doi.org/10.5194/os-16-799-2020

Nash, J. D., Kilcher, L. F., & Moum, J. N. (2009). Structure and composition of a strongly stratified, tidally pulsed river plume. *Journal of Geophysical Research*, *114*(C2), C00B12. https://doi.org/10.1029/2008JC005036

Nash, J. D., & Moum, J. N. (2005). River plumes as a source of large-amplitude internal waves in the coastal ocean. *Nature*, *437*(7057), 400–403. https://doi.org/10.1038/nature03936

Pahlevan, N., Smith, B., Schalles, J., Binding, C., Cao, Z., Ma, R., et al. (2020). Seamless retrievals of chlorophyll-a from Sentinel-2 (MSI) and Sentinel-3 (OLCI) in inland and coastal waters: A machine-learning approach. *Remote Sensing of Environment*, *240*, 111604. https://doi.org/10.1016/j.rse.2019.111604

Ralston, D. K., Geyer, W. R., Lerczak, J. A., & Scully, M. (2010). Structure, variability, and salt flux in a strongly forced salt wedge estuary. *Journal of Geophysical Research*, *115*(C12), C06005. https://doi.org/10.1029/2009JC006061

Rodriguez, A. R., Giddings, S. N., & Kumar, N. (2018). Impacts of nearshore wave-current interaction on transport and mixing of small-scale buoyant plumes. *Geophysical Research Letters*, *45*(16), 8379–8389. https://doi.org/10.1029/2018GL078328

Spicer, P., Cole, K. L., Huguenard, K., MacDonald, D. G., & Whitney, M. M. (2021). The effect of bottom-generated tidal mixing on tidally pulsed river plumes. *Journal of Physical Oceanography*, *51*(7), 2223–2241. https://doi.org/10.1175/JPO-D-20-0228.1

Stommel, H., & Farmer, H. G. (1952). *On the nature of estuarine circulation. Part 1 (chapters 3 and 4)*. Woods Hole Oceanographic Institution MA.

Umlauf, L., & Burchard, H. (2003). A generic length-scale equation for geophysical turbulence models. *Journal of Marine Research*, *61*(2), 235–265. https://doi.org/10.1357/002224003322005087

Warrick, J. A., & Fong, D. A. (2004). Dispersal scaling from the world's rivers. *Geophysical Research Letters*, *31*(4), L04301. https://doi.org/10.1029/2003GL019114

Wheless, G. H., & Valle-Levinson, A. (1996). A modeling study of tidally driven estuarine exchange through a narrow inlet onto a sloping shelf. *Journal of Geophysical Research*, *101*(C11), 25675–25687. https://doi.org/10.1029/96JC02529